Final Report

Grant/Contract Title: RELATIVISTIC MAGNETRON PRIMING EXPERIMENTS AND THEORY
Grant/Contract Number: FA9550-05-1-0087

<u>Personnel Supported</u>

<u>Faculty:</u> R.M. Gilgenbach and Y.Y. Lau
<u>Graduate Students and Postdocs:</u>
Brad Hoff, PhD, (Now Employed at AFRL, Kirtland AFB, NM)
Wilkin Tang, PhD, (Now Employed at AFRL, Kirtland AFB. NM)
Will White, PhD, (Now Employed at AFRL, Kirtland AFB. NM)
Du Pengvanich, PhD
V. Neculaes, PhD, (Employed by GE Research)
Michael Jones, PhD, (Employed by Sandia National labs)
Matthew Franzi
David Simon
Ian Rittersdorf
Ed Cruz
Peng Zhang
Sandu Varinder
<u>Undergraduate Students</u>
Arthur Holz
Abraham Thurtell
William Walsh
Lee Gunderson
Robert Steinbock

REPORT DOCUMENTATION PAGE

1. REPORT DATE *(DD-MM-YYYY)*	2. REPORT TYPE	3. DATES COVERED *(From - To)*
29-3-2010	Final	Jan. 1, 2005-Dec. 31-2009

4. TITLE AND SUBTITLE
RELATIVISTIC MAGNETRON PRIMING EXPERIMENTS AND THEORY

5a. CONTRACT NUMBER

5b. GRANT NUMBER
FA9550-05-1-0087

5c. PROGRAM ELEMENT NUMBER

6. AUTHOR(S)
R.M. Gilgenbach, Y.Y. Lau and R. Vidmar

5d. PROJECT NUMBER

5e. TASK NUMBER

5f. WORK UNIT NUMBER

7. PERFORMING ORGANIZATION NAME(S) AND ADDRESS(ES)
Nuclear Engineering and Radiological Scinces dept.
University of Michigan
Ann Arbor, MI 48109
University of Nevada Reno, Reno NV

8. PERFORMING ORGANIZATION REPORT NUMBER
10-1

9. SPONSORING/MONITORING AGENCY NAME(S) AND ADDRESS(ES)
Air Force Office of Scientific Research
875 North Randolph Street
Suite 325, Rm 3112
Arlington, VA 22203

10. SPONSOR/MONITOR'S ACRONYM(S)
AFOSR

11. SPONSOR/MONITOR'S REPORT NUMBER(S)
AFRL-OSR-VA-TR-2012-0103

12. DISTRIBUTION/AVAILABILITY STATEMENT
unlimited

13. SUPPLEMENTARY NOTES
none

14. ABSTRACT

Experiments and simulations were performed on magnetic priming to improve performance of relativistic magnetrons. Magnetic priming comprises N/2 azimuthal variations of magnetic field in N-cavity magnetrons. Experiments were performed on the 6-cavity, UM-L-3 magnetron at MELBA-C parameters of -300 kV, 1-5 kA and 300-500 ns. For unbalanced loads, magnetron performance was greatly improved by magnetic priming over baseline (uniform-B), including: a) reduction of start-oscillation time to 57% of baseline, b) Doubling of peak microwave power, and c) 20% increase in pulselength. Smaller improvements were observed for the balanced load case. Microwave window breakdown was eliminated by a redesign, tripling both the microwave power and pulselength. Theory included:
1. Discovery of unexpected effects of ions in magnetically insulated crossed-field gap. 2) Buneman-Hartree condition was critically re-examined in a cylindrical relativistic magnetron.

15. SUBJECT TERMS
High power microwaves, magnetron, crossed-field device

16. SECURITY CLASSIFICATION OF:			17. LIMITATION OF ABSTRACT	18. NUMBER OF PAGES	19a. NAME OF RESPONSIBLE PERSON
a. REPORT	b. ABSTRACT	c. THIS PAGE			Ronald Gilgenbach
unclassified	unclassified	unclassified	unlimited		19b. TELEPHONE NUMBER *(Include area code)* 734-763-1261

Reset

Experimental Research:
Magnetic Priming at the Cathode of a Relativistic Magnetron

B.W. Hoff, R.M. Gilgenbach, N.M. Jordan, Y.Y. Lau, E. Cruz, D. French, M.R. Gomez, J.C. Zier.,
T.A. Spencer[a], D. Price[b]
Plasma, Pulsed Power, and Microwave Laboratory
Department of Nuclear Engineering and Radiological Sciences
University of Michigan
Ann Arbor, MI 48109

[a] Air Force Research Laboratory, Kirtland AFB, Albuquerque, NM
[b] L-3 Communications, Titan Pulse Sciences Division, San Leandro, CA

Abstract
Experiments have been performed testing magnetic priming at the cathode of a relativistic magnetron to study the effects on high power microwave performance. Magnetic priming consists of N/2 azimuthal magnetic perturbations applied to an N-cavity magnetron for rapid generation of the desired number of electron spokes for the π-mode. Magnetic perturbations were imposed utilizing three high permeability nickel-iron wires embedded beneath the emission region of the cathode, spaced 120 degrees apart. Magnetic priming was demonstrated to increase the percentage of π-mode shots by 15% over the baseline case. Mean peak power for π-mode shots was found to be higher in the magnetically primed case by almost a factor of 2. Increases in mean microwave pulse width were also observed in the magnetically primed case when compared to the unprimed case (66 ns primed versus 50 ns unprimed). Magnetron starting current for the magnetically primed π-mode exhibited a reduction to 69% of the unprimed baseline starting current.

I. Introduction

Magnetrons are utilized extensively for commercial and military applications requiring power levels from kW to MW. There is continued interest in improving the performance of relativistic magnetrons, which operate at power levels ranging from 100's of MW to GW, in a number of areas [5, 6]. These areas of improved performance include mode control, peak power, start-oscillation time, and pulse length. One technique that has emerged as a promising technique to enhance magnetron performance is "magnetic priming".

Magnetic priming is defined as N/2 azimuthal magnetic perturbations applied to an N-cavity magnetron for rapid generation of the desired number of electron spokes for π-mode. This magnetic priming technique was originally demonstrated in kW oven magnetrons by Neculaes *et al*. Simulations using the MAGIC particle in cell code by Jones *et al*. showed that the application of an idealized magnetic priming field yielded rapid growth of the π-mode and suppression of mode competition in a relativistic magnetron. Other magnetron priming techniques investigated in recent years include: cathode priming, multiple cathodes, "transparent" cathodes, electric priming at the anode, and a recent resurgence of interest in rf priming of magnetrons. In this paper we report experiments to test magnetic priming at the cathode of a relativistic magnetron.

In order to create the azimuthal variations in the magnetic field of the previous oven magnetron experiments, small rare-earth magnets were placed on the *outside* of the annular, permanent magnets that are standard on the devices. Relativistic magnetrons are bulkier than oven magnetrons and generally use large pulsed electromagnets. Scaling up the original magnetic priming method used in the oven magnetrons for use in a relativistic magnetron would require very large external priming magnets, which were judged to be impractical. In order to impose the magnetic field perturbations required for magnetic priming of relativistic magnetrons, new techniques are required.

The magnetic priming concept implemented in the UM/L-3 Titan relativistic magnetron places magnetic structures *within* the cathode. Because of the close proximity of the priming

structures to the cathode surface, the magnetic perturbations are strongest on the cathode and weakest at the anode. This is opposite to the original magnetic priming experiments on oven magnetrons, where the magnetic perturbation is strongest in the anode region but decreases toward the cathode region. The first magnetic priming scheme used in the UM/L-3 Titan relativistic magnetron consisted of three nickel-iron alloy (Hymu 80/Permalloy) wires embedded within the cathode. These wires were located directly under the cathode surface, centered under the emission region, and spaced 120 degrees apart (for N/2 symmetry in a six vane magnetron).

II. Experimental Description and Operating Parameters

The 6-vane, L-band magnetron and Marx-Abramyan Bank voltage source used for these experiments are the same as reported by Lopez *et al*.: the Michigan Electron Long Beam Accelerator-Ceramic insulator (MELBA-C). The UM/L-3 Titan relativistic magnetron is designed with a coupling cavity at the back of each anode resonator cavity which allows microwave radiation to directly couple out of any or all of the 6 resonator cavities. In these experiments, three output waveguides were attached to alternating cavities. Lucite windows were used at the vacuum barrier between the magnetron and the waveguides. All other coupling cavities were sealed with vacuum-tight metal plates.

Waveguide-A utilized a -50dB microwave power coupler for diagnostics and a water load. Waveguide-B was terminated in a water load. Waveguide-C connected the relativistic magnetron to a smaller priming magnetron (not used in this experiment) through a T/R switch (shorted through the center of the waveguide with a large-gauge metal rod to prevent power flow to the T/R switch and priming magnetron). It is important to note that this array of output waveguides and associated loads and shorts created asymmetric loading of the relativistic magnetron, not expected to be conducive to π-mode operation.

The relativistic Hull cutoff curve represents the minimum magnetic field required to maintain magnetic insulation for a given voltage drop across the anode-cathode gap. This critical magnetic field can be calculated using Eqn. (1).

$$ B_{Hull} = \frac{m_e c}{eD} \cdot \left(\frac{2eV}{m_e c^2} + \left(\frac{eV}{m_e c^2} \right)^2 \right)^{\frac{1}{2}} \tag{1} $$

In Eqn (1), m_e and e are the rest mass and charge of an electron, respectively, c is the speed of light, and V is the voltage drop across the anode-cathode gap. D is the effective gap distance, defined by equation (2), in which r_a and r_c are the anode inner radius and cathode outer radius, respectively.

$$ D \equiv \frac{\left(r_a^2 - r_c^2 \right)}{2r_a} \tag{2} $$

Each of the Buneman-Hartree resonance lines describes the requirements on the voltage applied across the anode-cathode gap of a magnetron and the applied magnetic field to maintain synchronism between the electron spoke velocity and the phase velocity of the RF wave for a given mode. Equation (3) exhibits the relationship between the Buneman-Hartree voltage and magnetic field values, V_{BH} and B_{BH}.

$$ V_{BH} = B_{BH} D V_{ph}^n - \frac{m_e c^2}{e} \cdot \left(1 - \left[1 - \left(\frac{V_{PH}^n}{c} \right)^2 \right]^{\frac{1}{2}} \right) \tag{3} $$

The term V_{ph}^n, in Eqn. (3), represents the phase velocity for the *n*th azimuthal mode and is given by Eqn. (4). In Eqn. (4), ω_n is the angular frequency of the slow wave and n is the mode number (i.e., for a 6 vane magnetron n=1 for the π/3-mode and n=3 for the π-mode).

$$ V_{ph}^n = \omega_n r_a / n \tag{4} $$

Input current and voltage from MELBA are monitored by a Rogowski coil and copper-sulfate filled voltage-divider, respectively. A Pearson current transformer around the output lead for the endloss current collector detects the endloss current leaking out of the interaction space. Microwave power is sampled by a -50 dB coupler in waveguide-A. The signal is then passed through a series of additional attenuators and measured by a microwave diode detector. The signal from the "zero-area" B-dot loop is heterodyned with a local oscillator, then run through a Time Frequency Analysis (TFA) algorithm.

The cathode employed in this series of magnetic-priming experiments consisted of a grooved, aluminum support rod surrounded by an aluminum sleeve and connected between two electrostatic endcap-balls. The grooves were machined such that the magnetic wires placed in them were held against the inner wall of the cathode sleeve. Up to three magnetic wires of lengths ranging up to 25.8 cm can be mounted in the grooved support rod. For these initial experiments, three, 4-cm long wires with a diameter of 0.25 cm were utilized. The wires were composed of a high permeability nickel-iron alloy (Hymu 80/Permalloy).

The presence of the cathode sleeve allowed for the baseline and magnetic priming cases tested in this experiment to be electrostatically identical, so only the effects of the magnetic perturbations could be studied. The cathode sleeve itself had an outer diameter of 1.27 cm and a thickness of 0.086 cm. The emission region on the cathode sleeve was etched by the Ablation-Line-Focus (ALF) process over a region which was 1.67 cm long and centered axially within the relativistic magnetron anode block. The magnetic priming portion of the cathode assembly was then attached to a cathode extension stalk connected to the output of MELBA-C. For the magnetically primed experiments, once loaded into the magnetron, the cathode was rotated such that the priming wires were angularly aligned with three of the anode vanes.

Magnetostatic measurements at the cathode surface found the perturbation to be about 2% of the baseline field. Because the cathode sleeve is thin and the magnet pulse is long (~15 ms), the shielding effect of the sleeve was minimal due to magnetic diffusion. This magnetic perturbation amplitude is comparable to that calculated by Neculaes *et al*. for their oven magnetron priming experiments. Note, however, in our present experiments, this magnetic field perturbation is maximum on the cathode and decreases rapidly radially outward. Thus, the degree of magnetic priming in the present experiments is substantially weaker that that in Neculaes' experiments on oven magnetrons, as the magnetic perturbation is minimum on the cathode, and increases rapidly toward the anode. Even with a substantially weaker magnetic priming in the present experiments on the relativistic magnetron, improvement over the unprimed case was indeed observed, as shown in the next section.

III. Experimental Results

Two data sets were taken during this experiment. The first data set utilized the three, 4-cm nickel-iron wires for magnetic priming at the cathode. The second data set represents a baseline run with no magnetic wires in the cathode. The parameter space of the magnetically primed and unprimed shots encompassed the Buneman-Hartree resonance line for the π and $2\pi/3$ modes. The MELBA-C Marx generator mean output voltage during the microwave pulses was measured to be -315 kV with a standard deviation of 9.8 kV. Magnetron shots were taken at magnetic fields ranging from 2.75 to 3.09 kGauss.

The frequency of the microwave pulse at peak power, plotted as a function of applied magnetic field was measured.   When evaluated over each entire data set, the magnetically primed relativistic magnetron operated in the π-mode for 57 percent of the shots. In the baseline case, the relativistic magnetron operated in the π-mode in only 42 percent of the shots. The 15% increase in π-mode shots in the magnetically primed configuration versus the baseline configuration demonstrates that magnetic priming at the cathode increases the probability of the magnetron starting up in a desired mode (in this case, the π-mode) instead of a less desirable competing mode, $2\pi/3$.

Peak microwave power versus pulse width was measured for all π-mode shots in the magnetically primed and unprimed configurations. In general, the π-mode shots in the magnetically primed case exhibited higher peak microwave power and longer pulses than the unprimed baseline case. Differences in peak microwave power and pulse width between π-mode data sets for the primed and unprimed cases were verified to be statistically significant to a significance level of 0.05 using a t-test. The magnetically primed π-mode shots exhibited, on average, nearly double the peak power of the unprimed shots (11.4 MW primed versus 6.5MW unprimed). Additionally, the mean microwave pulse width in the magnetically primed case was extended by approximately 15 ns over the baseline case.

In addition to showing longer microwave pulse widths, the magnetically primed relativistic magnetron also showed reductions in starting time and time to peak power for π-mode shots. For these experiments, magnetron starting time was defined as the difference between the time the MELBA-C voltage pulse reached 10% of maximum value until the time at which the heterodyned microwave signal became detectable above the baseline noise. Time to peak power was defined as the difference between the time the MELBA-C voltage pulse reached 10% of maximum value until the time that the measured microwave signal reached maximum amplitude. Plots comparing the magnetron π-mode starting time and time to peak power of the magnetically primed and unprimed data sets were measured. Differences between the primed and unprimed sets in starting time and time to peak power were verified to be statistically significant to a significance level of 0.05 using a t-test. Mean starting time for the magnetically primed case was found to be less than that of the baseline case by 42 ns (27%). The magnetically primed case also showed a modest reduction of 33 ns (12%) in time to peak power when compared to the unprimed baseline case.

Mean magnetron starting currents for the magnetically primed and unprimed π-mode shots were compared. For this experiment, starting current was defined as the value of the magnetron entrance current at the time that the heterodyned microwave signal became detectable above the baseline noise. Starting currents in the magnetically primed case were significantly lower than those in the unprimed case. Mean starting current for the primed data set was found to be 1.04 kA with a standard deviation of 0.40 kA. Mean starting current for the unprimed data set was measured to be 1.50 kA with a standard deviation of 0.37 kA. At a significance level of 0.05, the difference in mean starting current between these two data sets was verified to be statistically significant using a t-test. Thus, for this experiment, magnetic priming was shown to reduce the mean magnetron starting current to 69% of the unprimed baseline value.

IV. Discussion

The initial simulation work involving magnetic priming of a relativistic magnetron performed by Jones *et al*. utilized a number of idealizations when compared to the actual experiment. In order to reduce simulation run time, the simulation magnetron utilized a larger cathode diameter (approximately three times the experimental diameter) and conformal anode vanes instead of the rounded vanes on the experiment. Additionally, the coupling cavities and load array in the present experiment were omitted. The experimental voltage rise time is on the order of 100 ns. In the simulations the full voltage is applied over the course of a few ns as a fast ramp.

The idealized magnetic priming field imposed in the simulations was of the form

$$B_z(\theta) = B_0 \cdot \left\{ 1 + \frac{\alpha}{2} \sin\left[n(\theta + \varphi) \right] \right\} \tag{5}$$

where B_0 is the base magnetic field, α is the magnetic priming strength, *n* is the number of azimuthal perturbations and φ is the phase of the magnetic field with respect to the anode vanes. Values for α, *n*, and φ used in the simulations were 0.3, 3, and 0, respectively. It is evident from Eqn. (5) that the idealized azimuthal magnetic perturbations in B_z did not vary as a function of radius from the cathode or location along the z axis. In the experiment, magnetic perturbations are localized around the emission region of the cathode since they are created by the finite

magnetic wires embedded in the cathode. The magnetic perturbation amplitude caused by the wires was also much milder than that imposed in the simulations (2% in the experiment versus 30% in the simulation).

Due to the idealizations used in the magnetic priming simulations of the UM/L-3 Titan relativistic magnetron, direct quantitative comparisons cannot be made between the simulations and the experiment; however, results from the magnetic priming experiments show many of the same trends as those demonstrated in the magnetically primed simulation magnetron. The two most notable effects seen by Jones *et al.* in the magnetic priming simulations was more rapid growth of the π-mode in the primed case and suppression of unwanted modes.

The magnetic priming simulations demonstrated dramatic reductions in π-mode start-oscillation time (primed starting time was 64% less than the unprimed case). In the experiment, mean π-mode starting time was reduced by 27%. Experimental results showed an increase in the percentage of π-mode shots (and consequently a reduction of 2π/3-mode shots) in the magnetically primed case when compared to the unprimed case. This experimental finding agrees with the demonstration of suppression of the 2π/3-mode in the simulations.

Differences in microwave output power between the primed and unprimed simulation magnetrons are not reported by Jones *et al.* Previous work involving the magnetic priming of kW oven magnetrons showed modest reductions in steady state π-mode output power (10%-20%) in the magnetically primed case when compared to the unprimed case. Experimental results from the magnetically primed case for the UM/L-3 Titan relativistic magnetron showed an increase in both mean microwave peak power (11.4 MW primed versus 6.5 MW unprimed) and microwave pulse width over the unprimed case for the π-mode. Although the relativistic magnetron is operated in a pulsed mode, as opposed to CW, the general trend of reduced microwave output power seen in the oven magnetron experiments was expected to be observed. However, it should be noted that unprimed oven magnetrons operate close to their peak efficiency of more than 80%. By contrast, unprimed relativistic magnetrons operate near 30% efficiency. Therefore, relativistic magnetrons possess much greater potential for efficiency enhancement than other magnetrons.

The oven magnetrons used in the work by Neculaes et al. were "locked" into the π -mode in both the primed and unprimed cases (with a consistent center frequency for the microwave output). The reduction in efficiency seen in the oven magnetron experiments was due to the reduction of the overall magnetic field. For a given magnetic field setting, the relativistic magnetron has a significant amount of shot to shot frequency variation. Varying degrees of mode competition likely contribute to this variation. While the presence of magnetic materials within the relativistic magnetron would cause a slight reduction in the overall magnetic field in the interaction, the effect of the primed magnetic field perturbations "locking" the magnetron more effectively into the pi-mode is probably a much more significant factor. If the oven magnetron had been completely "locked" into the pi-mode in both the primed and unprimed cases, it is likely that slightly lower efficiency would be observed due to the reduction of the overall magnetic field due to the presence of the magnetic wires.

The discrepancy between the power trends in the oven magnetron and relativistic magnetron could also be related to the effects of the asymmetric loading on the baseline π-mode operation of the relativistic magnetron. It should be noted that preliminary data from unprimed shots performed in a balanced load configuration (with all three waveguides the same as waveguide-A) showed single arm power outputs averaging over 20 MW in π-mode operation. It is possible that π-mode operation in the non-ideal operating conditions created by the asymmetric loading may be more easily influenced by magnetic priming at the cathode than π-mode operation in a balanced load configuration. Further experiments comparing magnetically primed versus unprimed operation in a balanced load configuration are necessary to explore this issue.

Future research will perform magnetic priming experiments using a balanced load configuration. Effects of larger perturbations created by longer wires embedded in the cathode will be explored. Modifications to the UM/L-3 Titan relativistic magnetron anode block allow for magnetic perturbations to be introduced at the anode vane surfaces. Experiments combining

magnetic priming at the cathode and the anode will be performed. Continued simulation and experimental work will explore additional novel magnetic priming concepts for implementation in relativistic magnetrons.

THEORETICAL RESEARCH

Three accomplishments on the theoretical study of the relativistic magnetron may be listed:

1. The unexpected effect of ions in a magnetically insulated crossed-field gap was discovered.
2. Electron multiplication at the triple point was analyzed.
3. The Buneman-Hartree condition was critically re-examined.

1. Using a single particle orbit model, shear flow model, and particle-in-cell simulation, we found that, in general, the presence of ions in a crossed-field gap always increases the electrons' excursion toward the anode region, regardless of the location of the ions. Thus, the rate at which the electrons migrate toward the anode, which is a measure of the diode closure rate, is related to the rate at which ions are introduced into the crossed-field gap. This anode migration of electrons is unrelated to crossed-field ambipolar diffusion. This unexpected phenomenon may well be a key factor to pulse shortening in relativistic magnetrons and is published in Y. Y. Lau, J. W. Luginsland, K. L. Cartwright, and M. D. Haworth, "Role of ions in a crossed-field diode," Phys. Rev. Lett. **98**, 015002 (2007).

2. We calculate the orbit of the first generation electrons at a triple point, which is directly relevant to the metal-oxide junction cathodes used in the UM-L3 relativistic magnetron. We found that, despite the mathematically divergent electric field at the triple point, significant electron yield most likely results from secondary electron emission when the seed electrons strike the dielectric. Our analysis gives the voltage scale in which this electron multiplication may occur. It also provides an explanation on why certain dielectric angles are more favorable to electron generation over others, as observed in previous experiments. This theoretical study was published in N. M. Jordan, Y. Y. Lau, D. M. French, R. M. Gilgenbach, and P. Pengvanich, "Electric field and electron orbits near a triple point," J. Appl. Phys. **102**, 033301 (2007).

3. We critically re-examined the Buneman-Hartree condition in a cylindrical relativistic magnetron using both the conventional single particle model, and the Brillouin flow model. These two models yield the same result for the Buneman-Hartree condition only in the limit of a planar magnetron. When b/a = 1.3, where a is the cathode radius and b (> a) is the anode radius, the difference in the two models becomes significant. When b/a = 4, the difference is acute; the Buneman-Hartree magnetic field, at a given voltage, in the Brillouin flow model exceeds four times that in the single particle model. Such a difference is always present, whether the voltage is relativistic or not. These results are quantified for b/a >> 1 using Davidson's model, conveniently cast in terms of the normalized gap voltage and normalized magnetic flux imposed on the cylindrical magnetron. A comparison with the University of Michigan/L-3 relativistic magnetron experiments is given. This work was published in Y. Y. Lau, J. W. Luginsland, K. L. Cartwright, D. H. Simon, W. Tang, B. W. Hoff, and R. M. Gilgenbach, "A re-examination of the Buneman-Hartree condition in a cylindrical smooth-bore relativistic magnetron," Phys. Plasmas **17**, 033102 (2010).

Three Dimensional Simulation of Magnetic Priming of a Relativistic Magnetron

B. W. Hoff[1,2], M. Franzi[1], R. M. Gilgenbach[1], Y. Y. Lau[1]

[1] Plasma, Pulsed Power, and Microwave Laboratory, Department of Nuclear Engineering and Radiological Sciences, University of Michigan, Ann Arbor, MI 48109 USA
[2] Air Force Research Laboratory, High Power Microwave Division, Directed Energy Directorate, Kirtland AFB, Albuquerque, NM 87117 USA

Abstract

Using a hybrid approach, three dimensional simulations of magnetic priming of a relativistic magnetron have been performed. The primed magnetic field values were calculated using a magnetostatics code (Magnum) then imported into a particle-in-cell code (Magic PIC) and run for the case of a six vane relativistic magnetron. The magnetically perturbative structures chosen for implementation in these simulations were sets of three high permeability wires of various lengths which would be placed within the cathode, the anode, or, in the combined case, both the cathode and anode.

In the best performing cathode wire case (three 4 cm wires), magnetic priming was found to reduce the start-oscillation time of the magnetron to 50% that of the unprimed case. When wires were embedded in both the cathode and the anode, the best performing case (4 cm cathode wires and 4 cm anode wires) was found to start oscillating in 30% of the start-oscillation time of the unprimed case. Magnetically primed magnetron cases were found to exhibit reduced equilibrium power levels, when compared with the unprimed case.

Discussion and Conclusions

Previous simulation work involving magnetic priming of relativistic magnetrons incorporates a number of assumptions that do not address effects that result from the use of finite magnetic structures to impose the B-field perturbations necessary to implement the technique. Using a hybrid approach, the magnetic priming field values were calculated using a magnetostatics code (Magnum) then imported into a particle-in-cell code (Magic PIC) and run for the case of a six vane relativistic magnetron. The magnetically perturbative structures chosen for implementation in these simulations were sets of three high permeability wires of various lengths which would be placed within the cathode, the anode, or, in the combined case, both the cathode and anode.

In all three general cases (magnetic priming at the cathode, magnetic priming at the anode, and magnetic priming at the cathode and anode), the magnetostatic simulation results showed that at the center of the wire lengths (Z=0), large perturbations in the Z component of the magnetic field exist, while perturbations in the θ and R components are negligible. Toward the ends of the ends of the wires, however, the perturbations in the θ and R magnetic field components were found to be over three times greater than the perturbations in B_z. In the case of magnetic priming at the cathode, the θ and R components of the magnetic field, which were largely ignored in previous simulation work, are likely to be strong contributors to magnetic priming effects in situations where the priming structure lengths are on the same order as the length of the electron emission region of the cathode.

In the PIC simulations of magnetic priming at the cathode, the 4 cm wire case showed the best overall performance. The presence of the 4 cm wires (in the $\mu_r = 500$ wire case) reduced the start-oscillation time of the primed magnetron to half that observed in the unprimed baseline case. While magnetic priming was shown to dramatically reduce the start-oscillation time of the magnetron, this improvement was realized at the cost of reduced output power.

The simulated magnetron was found to perform progressively worse as the magnetic priming wire lengths were increased beyond the optimal length, to the eventual point of failure to start up. Excessive magnetic priming wire lengths move the zones of high B_r and B_θ perturbations away from the emission region of the cathode and also cause an average

9

suppression of the B_z magnetic field around the cathode in a region long enough to cover both electrostatic end hats. This effect can alter the electron orbits in the vicinity of the cathode and allow larger amounts of current to escape around the end hats. These effects are likely to be the primary causes of the magnetron's failure to start up in the magnetic priming at the cathode cases using wires longer that 8cm.

When three 4 cm cathode wires were paired with sets of wires embedded in the anode block, further reductions in startup time were observed over those realized in the 4 cm magnetic priming at the cathode case. In the best performing combined magnetic priming case (4cm wires in the cathode and 4 cm sires in the anode), the magnetron start-oscillation time was reduced by 100 ns from the 4 cm cathode wire case. Additionally, the equilibrium power in the best performing combined anode and cathode case was observed to have the same equilibrium power output as the best performing magnetic priming at the cathode case (4 cm cathode wires, $\mu_r = 500$).

Magnetic priming simulations utilizing only anode wires were found to perform poorly when compared to the cathode wire cases and the combined cathode and anode wire cases. Reductions in magnetron start-oscillation time were observed in the longest anode wire cases (8 cm and 10 cm wires), but the output power of the magnetron was found to be significantly reduced compared to the baseline case. The steady-state magnetron output power in the 4 cm anode wire case was observed to be approximately the same as that in the best performing cathode wire case and combined cathode and anode case, but showed no reductions in start-oscillation time.

Although the simulations presented in this report incorporate physically realizable magnetic priming geometries, these simulations still involve a number of simplifications and assumptions that prevent direct quantitative comparisons from being made between the simulation results and the previously published experimental case. The simulation Bz perturbations were chosen to have approximately the same amplitude as the perturbations used in the simulations of Jones et. al. (on the order of 30% of the magnitude of the unprimed magnetic field). Pulsed magnetic field measurements performed in the experimental configuration indicated magnetic perturbation amplitudes that were approximately an order of magnitude less than the simulation perturbation amplitudes. Other differences between the experimental configuration used by Hoff, et. al and the 3D simulations include cathode size (larger cathodes used in the simulations to reduce run-time), applied voltage waveform (in the simulations, voltage was ramped to the desired value over a few RF cycles, while the voltage rise time in the experiment was around 100 ns, and microwave loading scheme.

Although the quantitative comparisons are not feasible, qualitatively the 3-D magnetic priming simulations presented in this paper showed many of the same trends observed in previously published simulation and experimental priming results. The simulation results of Jones and Luginsland and the experimental results of Neculaes and Hoff all show that magnetic priming increases the growth rate of the π mode in both relativistic and conventional oven magnetrons. This effect was also seen in the wire-based magnetic priming simulations presented. With the exception of the 8 and 10 cm anode wire cases, all magnetic priming simulations which started oscillating showed faster π-mode growth over the unprimed case, even in cases where the magnetron oscillation eventually died out due to excessive end loss current.

The 3-D wire-based magnetic priming simulations all showed reductions in magnetron output power, when compared to the baseline case. The oven magnetron simulations of Luginsland and the experimental work performed by Neculaes both display this trend; however the relativistic magnetron simulations by Jones and the experimental results by Hoff do not. The discrepancy in relativistic magnetron output power trends between the 3-D wire results and the 2-D simulations of Jones are likely due to end loss current effects. Magnetic field distortions along the length of the magnetron Z-axis that would result in increased end loss current from the cathode cannot be taken into account in 2-D geometry. The discrepancy in power trends between the 3-D simulation results and the relativistic magnetron experimental results may be due to the unbalanced loading scheme used in the experiment. If the output waveguide loading

scheme used is detrimental to π mode operation, magnetic priming might allow for the increase in power over the unprimed magnetron operation that was observed in the experiment. Additionally, in light of recent work by Hoff, et. al. breakdown of the microwave windows during the magnetic priming experiments, might be a contributing factor to the observed power trend discrepancy between the experiment and the 3-D simulations.

SUBCONTRACT FINAL PROGRESS REPORT

Contract/Grant Title: X-Ray Effects on Window Breakdown in Air
Contract/Grant #: FA9550-05-1-0087
Reporting Period: 1 Feb 2005 to 31 Oct 2009

Microwave breakdown of air on the air side of a microwave transmission window was investigated on the basis of an air-chemistry code and on the x-ray effects generated by a HPM device. X-rays as shown in Fig 1 irradiate the microwave window by a direct line of sight path and via channeling through the transmission waveguide. The early work on microwave breakdown is summarized in a time to avalanche curve that is a function of the effective reduced electric field (E/N) of microwaves (electric field divided by gas number density). That early result is summarized in a subhead on Time to Avalanche. Fundamental to the time to avalanche is the existence of a single free electron that initiates the avalanching process. The avalanche or gas breakdown has also been investigated by Kim and Verboncoeur[1] as an effect generated by a multipactor model that also requires a seed electron to initiate the process. The existence of a seed electron is postulated for both the high E/N and multipactor models but little has been brought forward to quantify the generation or presence of free electrons on the air side of the microwave transmission window prior to the arrival of an intense microwave pulse. The current research addresses the generation of free electrons from x-rays produced by a HPM machine.
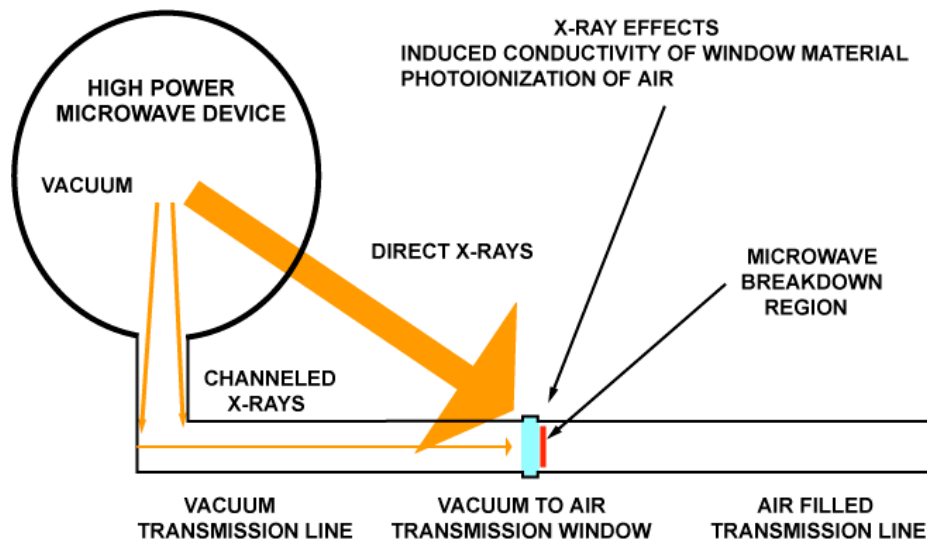

Figure 1 X-ray irradiation of transmission window region.

Theoretical and experimental research has been conducted to relate the operation of a HPM device to the subsequent generation of x-rays and the subsequent effects on window material and air near the window. It is readily accepted that x-ray generation occurs when HPM machines operate and that there will be some effects on the window and air, but the magnitude of the effects in the context of a practical machine are not well quantified. To quantify x-ray production in typical HPM devices, measurements were conducted on a 100 kV electron source at University of Nevada, Reno, that operates at approximately 2 mA. Because x-rays production is proportional to electron beam current and roughly proportional to beam energy from 0.1-1 MeV for aluminum and iron, results can be scaled up to the operating currents and beam energy found in a specific HPM device.

X-Ray Volumetric Ionization Rate. Part of the energy dissipated by x-rays in passing through matter produces ionization within the medium of propagation. Photo-interaction tables quantify the coefficients relating the total absorption, photoelectric effect, and other mechanisms.

12

For x-rays below 100 keV, the photoelectric effect is dominant. Because an instrument to measure the ionization rate is a custom rather than a commercial device, an indirect method of measuring the volumetric ionization rate at an arbitrary reference point r_1, $R(r_1)$ was developed. Theory relating the count rate, C_{det}, of a thallium activated sodium-iodine crystal, NaI(Tl), detector to the x-ray flux is well developed. The same theory is applied to x-ray ionization in air. Because the ionization rate is proportional to the x-ray flux, the x-ray flux can be estimated from a detector count rate and its physical parameters then used to solve for the volumetric ionization rate. The equation developed is for a thick detector that stops all the photons at energies below its threshold setting. The ionization of air due to its low density is a thin medium. The volumetric ionization rate is

$$R(r_1) = C_{det}(r_1) \frac{Y_{air} \left(\mu_{tr} / \rho \right)_{air} \rho_{air}}{\eta_{det} A_{det}} \tag{1}$$

where Y_{air} is number of electron-ion pairs generated per x-ray photon, $(\mu_{tr}/\rho)_{air}$ is the photoelectric absorption coefficient, cm^2/g, ρ_{air} is the density of air , g/cm^3, η_{det} is the absolute efficiency of an x-ray photon producing a count in the photomultiplier in the detector, and A_{det} is the area of the NaI(Tl) crystal pointing towards the x-ray source, cm^2. If all quantities are measured in cgs units the volumetric count rate has units of $1/cm^3$-s. Because the average x-ray produced by an electron beam source is approximately one half of the electron beam energy, V_{beam}, and the energy to generate an electron ion pair in air is approximately 34 eV per electron-ion pair, the value of Y_{air} (= $V_0/34$ eV) is 1,470. Although photoelectric absorption is only 10% of the total absorption coefficient at 50 keV, the major process scatters the x-rays that can subsequently initiate additional photoelectric absorption events. The absolute efficiency for a NaI(Tl) detector is approximately 0.05, which included light generation, light collection, and pulse generation via a photomultiplier.

The relationship between count rate and volumetric ionization rate is based on a single energy for x-rays. A better analysis would involve incorporating an x-ray spectrum into the analysis. In doing so, the theoretical estimate is more exact but the experimentalist needs to measure the spectrum produced and account for alteration of the spectrum due to the materials the x-rays interact with. One then finds that a measurement of the spectrum must be made next to the transmission window during a HPM pulse. Pulse height analysis of the detector output is often used to quantify the spectrum but may not be suitable for a short-duration pulsed source. By using layers of absorbing material in front of the detector one can determine the spectrum from many individual x-ray pulses.

X-Ray Detection System. An x-ray counting system capability was developed based on a Ludlham Model 44-2 tube with a NaI(Tl) crystal detector. The equipment utilized is shown in Fig. 2 and utilizes a SR445A 350-MHz preamplifier and a SR430 Multi-Channel Scaler. The SR430 can be triggered to provide a real-time pulse counting capability. The SR430 derived its trigger pulse from the signal generator used to trigger a Kimball EGH 8201 electron-beam source. The trigger pulse has a 5-ms delay before the beam turns on to provide a reference period prior to initiating an electron-beam pulse of 7-ms duration.

Because the threshold setting of the SR430 strongly influences its count rate, the detector was calibrated using a 1 µCi and 10 µCi ^{137}Cs source that has a strong x-ray line at 662 keV. Additional tests verified the system was operating without pulse pileup and operated within its 100 MHz pulse counting rate. Initial results with a 100 keV electron beam with the detector threshold set for 100 keV produced very low count rates and failed to detect any x-ray generation within the tank. This null result indicated x-ray production was most likely occurring at approximately 50% of the electron-beam energy. The detector threshold was lowered so that the detector was sensitive to 50 keV and higher energy x-rays and substantial x-ray count rates were detected during electron-beam pulses.
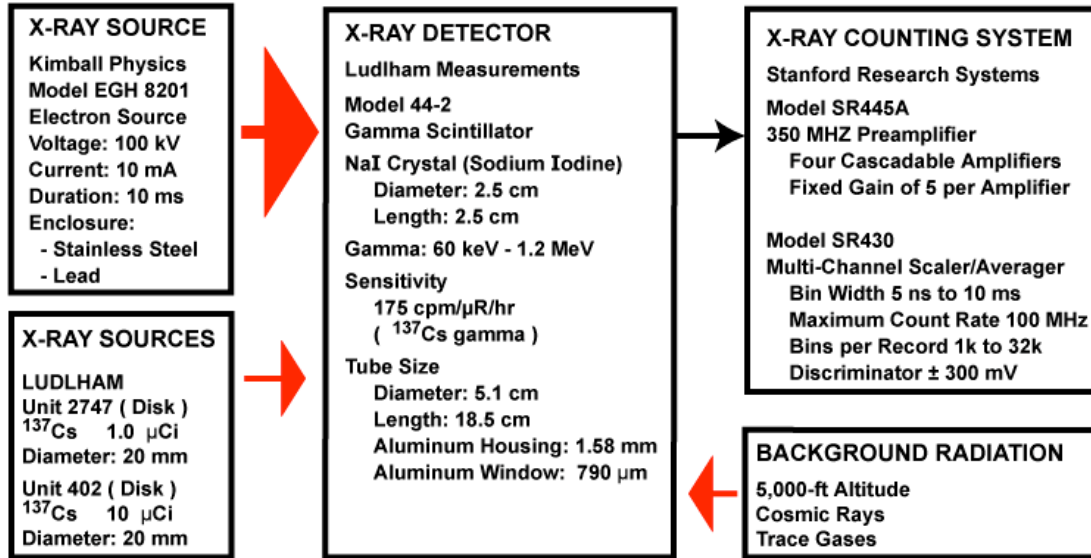
X-RAY SOURCE

Kimball Physics
Model EGH 8201
Electron Source
Voltage: 100 kV
Current: 10 mA
Duration: 10 ms
Enclosure:
 - Stainless Steel
 - Lead

X-RAY SOURCES

LUDLHAM
Unit 2747 (Disk)
^{137}Cs 1.0 µCi
Diameter: 20 mm

Unit 402 (Disk)
^{137}Cs 10 µCi
Diameter: 20 mm

X-RAY DETECTOR

Ludlham Measurements

Model 44-2
Gamma Scintillator
NaI Crystal (Sodium Iodine)
    Diameter: 2.5 cm
    Length: 2.5 cm
Gamma: 60 keV - 1.2 MeV
Sensitivity
    175 cpm/µR/hr
    (^{137}Cs gamma)
Tube Size
    Diameter: 5.1 cm
    Length: 18.5 cm
    Aluminum Housing: 1.58 mm
    Aluminum Window: 790 µm

X-RAY COUNTING SYSTEM

Stanford Research Systems
Model SR445A
350 MHZ Preamplifier
    Four Cascadable Amplifiers
    Fixed Gain of 5 per Amplifier

Model SR430
Multi-Channel Scaler/Averager
    Bin Width 5 ns to 10 ms
    Maximum Count Rate 100 MHz
    Bins per Record 1k to 32k
    Discriminator ± 300 mV

BACKGROUND RADIATION

5,000-ft Altitude
Cosmic Rays
Trace Gases

Figure 2 X-ray diagnostic equipment.

Pulsed X-Ray Measurements. The Kimball 8201 electron source and air-plasma test cell are shown in Fig. 3. Electrons are generated and accelerated in the large cylinder at the top of Fig. 3 then drift downward into the test cell. A second turbo pump and 4.5CF cross were added directly above the upper flange to provide pumping for a 0.5-mil aluminum transmission window bolted to the lower side of the upper flange. The source was covered by a sheet of ¼-inch lead rolled into a cylinder, with holes for turbo pumps. X-ray measurements were made inside the tank by removing one of the 4.5CF flanges on the circumference of the tank between the 8CF ports shown in Fig. 3. Other measurements were made at a height of 20 cm above the upper flange with the x-ray tube horizontal to the floor and pointing to the beam axis. Reference count-rate measurements for background radiation and ^{137}Cs sources of 1 µCi and 10 µCi were conducted for the discriminator settings and amplifier gain blocks used for the experiments.

AIR-PLASMA TEST CELL
 - INSIDE DIAMETER 36 inch, 91.44 cm
 - INSIDE HEIGHT 24 inch, 60.96 cm
 - VOLUME 24,430 in^3, 400.4 liter
 - VENDOR: NOR-CAL PRODUCTS

ELECTRON BEAM: EGH-8201
 - BEAM ENERGY: 10 keV to 100 keV
 - PULSED BEAM CHARACTERISTICS
     CURRENT: UP TO 20 mA
     PULSE WIDTH: 1 µs TO DC
     RISE/FALL: 200 ns
     REPETITION RATE: DC TO 5 kHZ
             500 kHz IN 1 ms BURST
 - BEAM UNIFORMITY: GAUSIAN
 - CATHODE: THORIA (ThO$_2$) COATED IRIDIUM
 - SPOT SIZE: 1 mm to 100 mm
 - VENDOR: KIMBALL PHYSICS

Figure 3. X-ray measurements using 100 keV electron source.

Measurements of x-ray production were taken over a two week period. The background radiation count rate at 5,000 ft was 30 counts/s and represents 340 pR/s. The x-ray tube was placed near to, far from, and inside the air-plasma test cell. An example of an x-ray pulse for the detector extending 2-inches into the tank resulted in the pulse shown in Fig. 3(a). The detector set for 50 keV saturated at a count rate over 500,000 counts/s. The detector count rate with the discriminator set for 100 keV was only a few counts per second. A 10 µCi ^{137}Cs source produces a count rate of 466,000 counts/s, so the pulse represents approximately 150 nR/s. The pulse in Fig. 3(b) at a distance of 1.5 m from the source was aligned with one of the turbo pumps and a hole in the lead shielding. Although the amplification unit was set differently, a comparison to a 10 µCi ^{137}Cs source indicates the pulse represents approximately 150 nR/s. When the detector was placed against the ¼-inch lead shield that encircles the electron-beam source, the count rate fell to 32,000 counts/mA-s, which is well below saturation, and represents 3.9 nR/mA-s. These measurements indicate a variation of an order of magnitude depending on the shielding present and whether a direct line of sight to the source or the electron beam transmission window was present. The measurements on a worst case basis represent approximately 2 nR/mA-s and a count rate of 30,000 counts/mA-s.
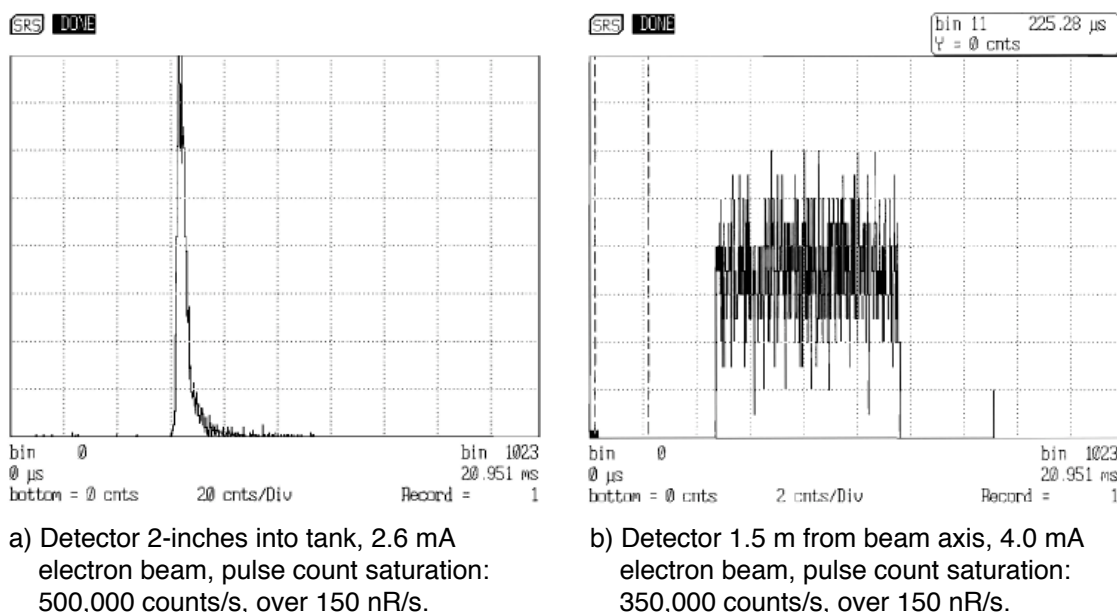

a) Detector 2-inches into tank, 2.6 mA electron beam, pulse count saturation: 500,000 counts/s, over 150 nR/s.

b) Detector 1.5 m from beam axis, 4.0 mA electron beam, pulse count saturation: 350,000 counts/s, over 150 nR/s.

Figure 4. X-ray measurements using 100 keV electron source.

Volumetric Ionization Rate. Coefficients used in evaluating the volumetric ionization rate are the coefficient for photoelectric absorption at 50 keV, $(\mu_{tr}/\rho)_{air}$ = 2.11 × 10^{-3} g/cm^2 , and the detector area A_{det} = 5.06 cm^2. Using an x-ray pulse rate of 30,000 counts/mA-s, the volumetric ionization rate at an altitude of 5,000 ft (ρ_{air} = 1.08 × 10^{-3} g/cm^3) is 3,970 electron-ion pairs/cm^3-s-mA. The background radiation count rate of 30 s^{-1} produces 3.9 electron-ion pairs/cm^3-s. At an altitude of 50,000 ft (ρ_{air} = 1.90 × 10^{-4} g/cm^3) the volumetric ionization rate is 69.8 electron-ion pairs/cm^3-s-mA.

In application to a HPM device operating at 50,000 ft a typical electron beam current is approximately 1 kA and the applied voltage is a few hundred keV. The volumetric ionization rate scales up to 69.8 × 10^6 electron-ion pairs/cm^3-s. This ionization rate is sufficient to provide one free electron in 14 ns. This is sufficient to initiate an electron avalanche discussed in the next section or provide the seed electron for the multipactor mechanism.

Time-to-Avalanche. The curves in Fig. 5 quantify the time it takes for a single seed electron to increase in number density as a function of time and applied E/N from 1.0 × 10^{-15} V-cm^2 to 1.6 × 10^{-15} V-cm^2. The curves are based on an air-chemistry code[2] developed to model ionization and deionization in air. When the electric field is less than 1.2 × 10^{-15} V-cm^2, the process of electron attachment to oxygen is the dominant process and the electron concentration is small. When the electric field increases such that E/N > 1.3 × 10^{-15} V-cm^2, the process of impact ionization of oxygen becomes the dominant process and the electron concentration increases to a large magnitude in a few hundred nanoseconds. For microwave propagation the additional electrons change the conductivity of air, which changes the impedance for microwave propagation. The change of impedance generally results in a partial reflection that further increases the electric field, E/N, and results in prompt breakdown.
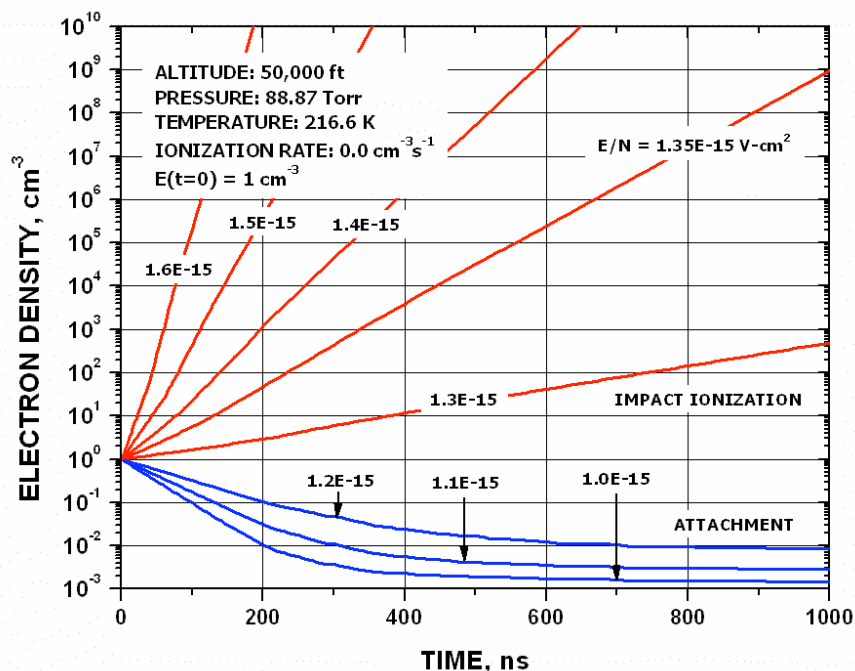

Figure 5. Time to avalanche as a function of E/N.

For a situation where the x-ray flux on the microwave transmission window is substantial and the volumetric ionization rate supports an initial condition of more than 1 electron/cm^3, the initial electron density can be set to 10 cm^{-3} or 100 cm^{-3} and the time scale shifted over. For example, an initial electron density of 100 cm^{-3} and E/N 1.3 × 10^{-15} V-cm^2, would have a time shift of 700 ns and the electron concentration would rise to 10^4 electrons/cm^3 in 700 ns.

INDUCED CONDUCTIVITY IN WINDOW MATERIALS. X-rays as noted in Fig. 1 and irradiate the microwave transmission window through direct or channeled radiation. If the intensity of x-rays is sufficiently high, there is a predictable change in the overall conductivity of transmission window materials such as glass and quartz[3-5], as shown in Fig. 6 from Ahrens and Wooten[3]. Changes in conductivity on the order of 10^{-16} 1/Ω-cm occur when the x-ray dose rate exceeds 1 R/s. The x-ray pulse measurements indicate a dose rate of 2 nR/mA-s. A HPM machine with current pulses of 1 MA would produce a dose rate of 2 R/s and may induce a conductivity effect. The effect is weak for the direct path shown in Fig. 1. Radiation that is channeled by the microwave waveguide may or may not be larger than the direct path. An x-ray counting experiment to quantify the dose rate at the transmission-window-to-air interface would provide measurements of both dose rate and volumetric ionization.
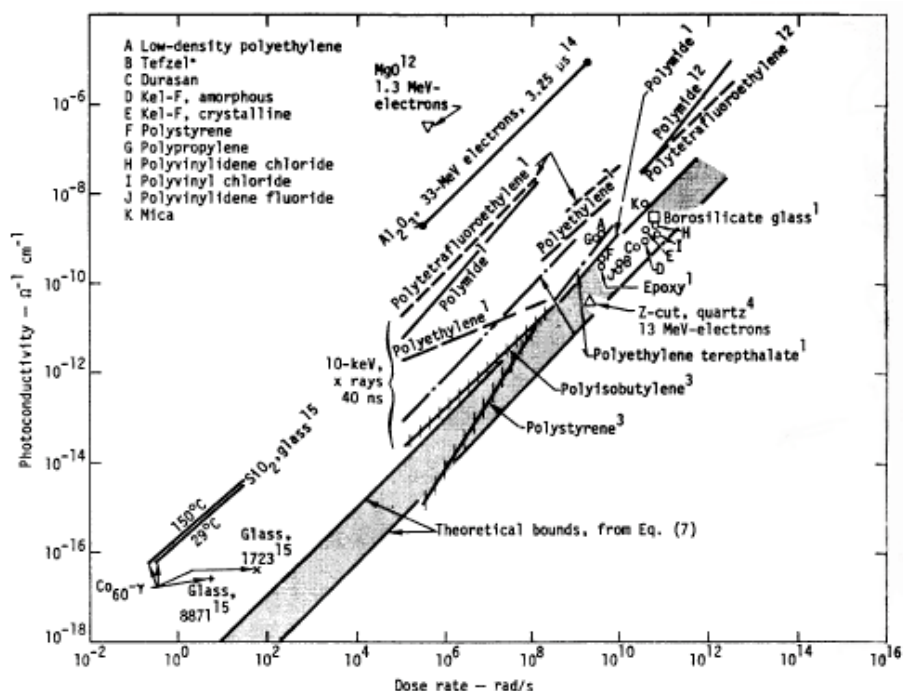
Figure 6. Theoretical and experimental induced photoconductivities in various engineering materials. Extracted from Ahrens, T. J., and F Wooten, "Electrical Conductivity Induced in Insulators by Pulsed Radiation," IEEE Transactions on Nuclear Science, Vol NS-23, No 3, pp 1268-1272, June 1976.

SUMMARY

Experimental and theoretical research quantified the approximate x-ray count rate and related it to the volumetric production rate of electron-ion pairs in air. For kA HPM machines there is sufficient volumetric ionization to support the production of 1 free electron in 14 ns. This is sufficient to initiate microwave breakdown of high E/N microwave pulses. An associated effect of induced conductivity in engineering materials indicates some effects would occur at dose rates above 1 R/s and may occur in a MA HPM machine. In a practical setting for a specific HPM machine, the results suggest it would be good practice to quantify the x-ray count rate at the microwave window-to-air interface and estimate the free electron production rate. If the rate is high, the window could be moved to a more favorable location with a lower x-ray flux.

PERSONNEL, INTERACTIONS, AND PUBLICATIONS

Personnel. The personnel for this subcontract consisted of one researcher as noted below.

Primary Personnel

• Robert J Vidmar, Principal Investigator

Students and Technical Support

• None

Interactions. Research conducted on this project was presented at the 62nd Gaseous Electronic Conference.

Conference Presentations

Vidmar, R.J., and A. Uppaluri, "X-Ray Induced Breakdown in Air with High Reduced Electric Field" Oral Presentation PW3.00004, 62nd Annual Gaseous Electronics Conference, 20-23 Oct 2009, Saratoga Springs, New York, Bulletin of the American Physical Society, Series II, at press, Oct 2009.

Vidmar, R.J., and A. Uppaluri, "X-Ray Induced Breakdown in Air at High Reduced Electric Field: Experimental Details" Poster Presentation URP.00082, 62nd Annual Gaseous Electronics Conference, 20-23 Oct 2009, Saratoga Springs, New York, Bulletin of the American Physical Society, Series II, at press, Oct 2009.

REFERENCES

1. Kim, H. C., and J. P.Verboncoeur, Time-dependent physics of a single-surface multipactor discharge, Physics of Plasmas, Vol 12, pp 123504-1-7, 2005.

2. Vidmar, R. J., and K. R. Stalder, "Air Chemistry and Power to Generate and Sustain Plasma: Plasma Lifetime Calculations," AIAA 2003-1189, p 8, Jan, 2003.

3. Ahrens, T. J., and F Wooten, "Electrical Conductivity Induced in Insulators by Pulsed Radiation," IEEE Transactions on Nuclear Science, Vol NS-23, No 3, pp 1268-1272, June 1976.

4. Frederickson, A. R., "Radiation Induced Currents and Conductivity in Dielectrics," IEEE Transactions on Nuclear Science, Vol NS-24, No 6, pp 2532-2539, Dec 1977.

5. Face, S. H., C. A. Eklund, and T. A. Stringer, "Measurement of Radiation Induced Conductivity for Hardened Cable Dielectric Materials at High Fluence," IEEE Transactions on Nuclear Science, Vol NS-30, No 6, pp 4450-4456, Dec 1983.